

RSC Advances



This is an *Accepted Manuscript*, which has been through the Royal Society of Chemistry peer review process and has been accepted for publication.

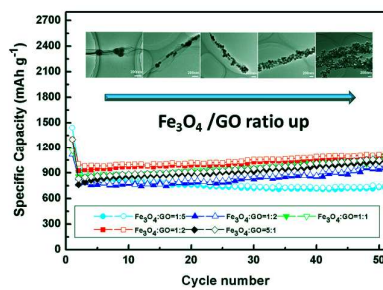
Accepted Manuscripts are published online shortly after acceptance, before technical editing, formatting and proof reading. Using this free service, authors can make their results available to the community, in citable form, before we publish the edited article. This *Accepted Manuscript* will be replaced by the edited, formatted and paginated article as soon as this is available.

You can find more information about *Accepted Manuscripts* in the [Information for Authors](#).

Please note that technical editing may introduce minor changes to the text and/or graphics, which may alter content. The journal's standard [Terms & Conditions](#) and the [Ethical guidelines](#) still apply. In no event shall the Royal Society of Chemistry be held responsible for any errors or omissions in this *Accepted Manuscript* or any consequences arising from the use of any information it contains.

Table of Contents

The mass ratio of $\text{Fe}_3\text{O}_4/\text{GO}$ plays an important role in determining the structure and the electrochemical performances of $\text{Fe}_3\text{O}_4 @\text{GNS}$.





Journal Name

ARTICLE

Controllable synthesis of graphene nanoscroll-wrapped Fe₃O₄ nanoparticles and their lithium-ion battery performances

Received 00th January 20xx,
Accepted 00th January 20xx

DOI: 10.1039/x0xx00000x

www.rsc.org/

Bingjun Yang,^{a,b} Jinping Zhao,^b Jiangtao Chen,^b Mu He,^a Shan Xu^{a*}

Abstract: In this work, a series of graphene nanoscroll (GNS)-wrapped Fe₃O₄ nanoparticles (NPs) composites (denoted as Fe₃O₄@GNS) are prepared by cold quenching of the mixed suspensions of water-dispersible Fe₃O₄ NPs and graphene oxide (GO) with different mass ratios in liquid nitrogen followed by a low-temperature thermal reduction. In all samples, it is interesting that Fe₃O₄ NPs are able to in-situ encapsulated completely in GNSs, forming a three-dimensional network consisted of fiber-like structure. The amount of Fe₃O₄ NPs wrapped with GNSs is in proportion to the mass ratio between Fe₃O₄ NPs and GO in the initial mixed suspension. As a new anode material of lithium ions batteries (LIBs), these Fe₃O₄@GNSs exhibit outstanding Li-ion storage characteristics. Among them, Fe₃O₄@GNS (Fe₃O₄: GO=2:1) electrode shows the best electrochemical properties, including excellent cycling stability with a reversible capacity of 1172 mAh g⁻¹ over 200 cycles at 100 mA g⁻¹ and 525 mAh g⁻¹ over 1000 cycles at 2 A g⁻¹, as well as superior rate performance with a reversible capacity of 648 and 480 mAh g⁻¹ at 2 and 5 A g⁻¹, respectively. Such high performance is very closed to the novel hybrid structure of Fe₃O₄@GNS as well as the optimal ratio between Fe₃O₄ and GO.

Introduction

Lithium ions batteries (LIBs) are considered as one of the most practical and effective technologies for portable electronic devices and electric vehicles (EVs).¹⁻⁴ However, it is still a great challenge to find novel electrode materials with improved performances.⁵ As promising anode electrodes, various transition metal oxides (e.g., SnO₂, NiO, Fe₃O₄, Fe₂O₃, etc.)⁶⁻¹¹ have attracted great attention due to their much higher specific capacities than commercial graphite (~372 mAh g⁻¹). Among these metal oxides, Fe₃O₄ has been widely studied because of its high reversible specific capacity (~1000 mAh g⁻¹), low cost, high corrosion resistance, world-wide abundance as well as environmentally-friendly properties.¹² However, Fe₃O₄ suffers from poor lithium ion kinetics and large volume change (~200%) during Li⁺ insertion/extraction, thus limiting its application as commercial LIBs anode.^{13,14} Therefore, two effective approaches have been employed to overcome the intractable problems. One is to employ nanosized Fe₃O₄ which

can provide short ion and electron transport pathways.^{15,16} Another is to construct carbon-Fe₃O₄ hybrid structures in order to enhance the electrical conductivity and the structural stability of Fe₃O₄.¹⁷⁻²⁰ Among various carbon materials, graphene have attracted significant attention because of its novel two-dimensional structure, superior electrical conductivity, high surface area and excellent chemical tolerance.^{21,22} Consequently, as a kind of potential anodes for LIBs, different graphene-Fe₃O₄ hybrid structures, including graphene-encapsulated Fe₃O₄,²³ graphene-wrapped Fe₃O₄,²⁴ graphene-mixed Fe₃O₄,²⁵ graphene anchored Fe₃O₄,²⁶ and graphene-laminated Fe₃O₄,²⁷ have been reported, and exhibited obviously improved electrochemical performances (capacity, rate capability as well as cycling stability).

Graphene nanoscroll (GNS), as a new member of graphene family, has been recently attracting great attention due to its novel structure and electronic property.²⁸⁻³⁰ GNS is a spirally wrapped graphene sheet with a one-dimensional tubular structure resembling that of a multiwalled carbon nanotube (MWCNT). It is conceivable that, if electro-active metal oxides are well wrapped into the interlayer galleries of GNSs, the volume change of metal oxides could be more effectively inhibited during the charge-discharge process compared with traditional graphene-encapsulated/or wrapped metal oxides, at same time GNS act as an effective network to promote ion and electron transport, resulting in the significant improvement in the Li storage performance. However, GNS-wrapped structures are very limitedly reported because metal

^a State Key Laboratory for Oxo Synthesis and Selective Oxidation, Lanzhou Institute of Chemical Physics, Chinese Academy of Sciences, Lanzhou 730000, P. R. China.

^b Laboratory of Clean Energy Chemistry and Materials, Lanzhou Institute of Chemical Physics, Chinese Academy of Sciences, Lanzhou 730000, P. R. China.

* Corresponding author. Tel.: +86-931-4968339; fax: +86-931-4968129. E-mail address: xushan@licp.cas.cn

Electronic Supplementary Information (ESI) available: [details of any supplementary information available should be included here]. See DOI: 10.1039/x0xx00000x

oxides are difficult to be filled into the interlayer galleries of GNSs.³¹ More recently, we have demonstrated a novel strategy for preparation of GNS by a simple cold quenching in liquid nitrogen.³² Furthermore, GNS-wrapped metal oxide nanoparticles (NPs) hybrid structure were in-situ prepared by precisely controlling the experimental conditions.³³

Herein, we prepared a series of graphene nanoscroll-wrapped Fe_3O_4 nanoparticles composites ($\text{Fe}_3\text{O}_4@\text{GNS}$) with different $\text{Fe}_3\text{O}_4/\text{GO}$ ratios by precisely adjusting the initial mass ratio of water-dispersible Fe_3O_4 NPs and GO. On this basis, the electrochemical properties of as-prepared composites were investigated using galvanostatic charge/discharge, Cyclic voltammetry (CV) and Electrochemical impedance spectroscopy (EIS) in order to systematically study the optimum design of component and structure as well as the corresponding influence on the electrochemical properties. The results show that Fe_3O_4 NPs are able to in-situ encapsulated completely in GNSs at same time forming a three-dimensional network consisted of fiber-like structure in all samples. Also, the mass ratio of $\text{Fe}_3\text{O}_4/\text{GO}$ plays an important role in determining the cycling and rate performances of final composites for LIBs anodes, and the optimum ratio is 2:1. This sample can deliver 1172 mAhg^{-1} at 100 mA g^{-1} after 200 cycles and 525 mA h g^{-1} even after 1000 cycles at 2 A g^{-1} , as well as superior rate performance with a reversible capacity of 648 and 480 mAh g^{-1} at 2 and 5 A g^{-1} , respectively.

Experimental

Preparation of GO sheets and Fe_3O_4 NPs

Firstly, GO sheets were synthesized from natural flake graphite (32 mesh) by a modified Hummers method.³⁴ Uniform Fe_3O_4 NPs were synthesized by a simple hydrothermal method as the previous report.^{35,36} Briefly, 1.35 g of $\text{FeCl}_3 \cdot 6\text{H}_2\text{O}$, 2.7 g of sodium acetate and 1.0 g of trisodium citrate were completely dissolved into 25 mL of ethylene glycol under vigorously stirring. After that, the mixed solution was immediately transferred in a Teflon-lined autoclave (with a volume of 50 ml) and then heated at $200 \text{ }^\circ\text{C}$ for 10 h. The precipitate was washed with ethanol and deionized water three times. Finally, the Fe_3O_4 NPs were obtained after vacuum dried at $25 \text{ }^\circ\text{C}$.

Preparation of $\text{Fe}_3\text{O}_4@\text{GNS}$ with different $\text{Fe}_3\text{O}_4/\text{GO}$ ratios

Firstly, 1.0 mg mL^{-1} Fe_3O_4 aqueous dispersion and 1.0 mg mL^{-1} GO suspension were prepared. Then, a series of mixed suspensions (placed in plastic tubes with a volume of 10 ml) with different mass ratios between Fe_3O_4 and GO ($\text{Fe}_3\text{O}_4:\text{GO}=1:5, 1:2, 1:1, 2:1$ and $5:1$) were prepared by mixing Fe_3O_4 dispersion and GO suspension with different volumes. After that, mixed suspensions were heated up to $80 \text{ }^\circ\text{C}$ before aid of sonication for 5 min, then rapidly put into liquid nitrogen. The completely frozen solids were suffered the vacuum freeze-drying to remove water. Finally, the products were obtained

by thermal-reduction at $300 \text{ }^\circ\text{C}$ in argon atmosphere for 3 hours.

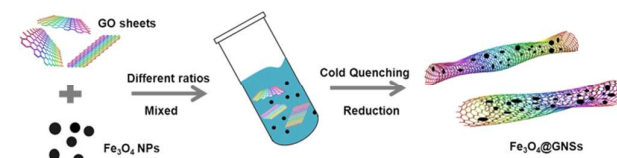
Characterization

The microstructure and morphology of as-synthesized samples was characterized by powder X-ray diffraction (XRD, $\text{CuK}\alpha$ radiation, Panalytical X'Pert Pro), field emission scanning electron microscope (FESEM, JSM 6701F) and transmission electron microscope (TEM, Tecnai G20). The amounts of carbon in different hybrid samples were tested by an elements analyzer (EA, VarioEL), and the Fe amounts were tested by an inductively coupled plasma-atomic emission spectrometry (ICP-AES, Agilent-725).

Electrochemical measurement

The working electrodes were prepared by using 9:1 in weight ratio of active material and binder (polyvinylidene difluoride, PVDF) in *n*-methyl-2-pyrrolidinone (NMP). Then the slurry was coated on a copper foil. The as-prepared electrodes were dried under vacuum at $110 \text{ }^\circ\text{C}$ for 10 h. Electrochemical test cells were assembled in an argon-filled glove box using coin-type half-cells (CR2032) with lithium foil as a counter electrode, using 1 mol L^{-1} LiPF_6 in ethylene carbonate (EC) and diethyl carbonate (DEC) (1 : 1, v/v) as the electrolyte. The assembled coin cells were tested in the voltage range of 0.01-3.0 V on a CT2001A cell test instrument (LAND Electronic Co.). The specific capacity was calculated based on the weight of active material. CV curves and EIS plots were recorded using an electrochemical workstation (CHI660D, Shanghai, China).

Results and discussion



Scheme 1 Schematic illustration showing the synthetic process of $\text{Fe}_3\text{O}_4@\text{GNS}$ with different $\text{Fe}_3\text{O}_4/\text{GO}$ ratios.

Scheme 1 is the schematic diagram of synthetic route of $\text{Fe}_3\text{O}_4@\text{GNS}$ with different $\text{Fe}_3\text{O}_4/\text{GO}$ ratios. Firstly, Fe_3O_4 NPs were prepared by a simple hydrothermal method.^{35,36} Figure 1a and b show SEM and TEM images of the as-prepared Fe_3O_4

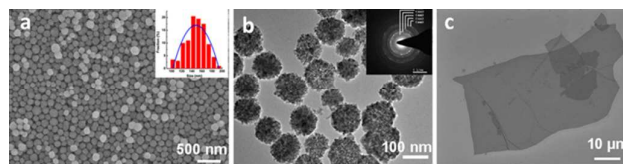


Figure 1 (a) SEM image of as-prepared Fe_3O_4 NPs, inset is the corresponding size distribution of as-prepared Fe_3O_4 , (b) TEM image of as-prepared Fe_3O_4 NPs, inset is the corresponding SAED, (c) SEM image of as-prepared GO sheet.

NPs. The size distribution of as-prepared Fe_3O_4 NPs (Figure 1a, inset) is in range of 140–180 nm. A high-resolution TEM image (Figure S1) further reveals that the particles are composed of nanocrystals with the size of about 10–15 nm. Selected-area electron diffraction (SAED) recorded on the edge of a Fe_3O_4 NPs shows polycrystalline-like diffraction, which suggesting that it consists of many magnetite nanocrystals (Figure 2b, inset). GO sheets were prepared according to the reported method,³⁴ as shown in Figure 1c. Then the plastic tube that loaded with mixed suspension of GO and Fe_3O_4 with different ratios were quickly immersed liquid nitrogen for cold quenching before heated up to 80 °C. The Fe_3O_4 NPs dispersed in the GO aqueous suspension might be wrapped with GO sheets during the GO rolling process. After that, frozen suspensions are freeze-dried, and final Fe_3O_4 @GNS products were obtained by thermally reduced. For convenience, Fe_3O_4 @GNS with different Fe_3O_4 /GO ratios (Fe_3O_4 : GO=1:5, 1:2, 1:1, 2:1 and 5:1, the ratio based on the raw materials in mass) was labeled as sample 1-5.

The synthesis parameters of Fe_3O_4 @GNS with different Fe_3O_4 /GO ratios and the element ratios of the samples were evaluated by EA and ICP-AES. As shown in Table 1, the content

Table 1 The synthesis parameters of Fe_3O_4 @GNS with different Fe_3O_4 /GO ratios and corresponding Fe and C elements content

	Fe_3O_4 /GO	Fe (%)	Fe_3O_4 (%)	C (%)	Fe/C	Fe_3O_4 /C
Sample 1	1:5	14.7	20.28	59.75	0.24	0.33
Sample 2	1:2	24.3	33.35	53.67	0.25	0.62
Sample 3	1:1	34.0	46.95	38.97	0.87	1.28
Sample 4	2:1	40.0	55.20	24.14	1.66	2.28
Sample 5	5:1	51.3	70.79	17.42	2.94	4.06

of Fe in sample 1-5 gradually increases and the C element decreases. The ratios of Fe_3O_4 to C for sample 1-5 are 0.33, 0.62, 1.28, 2.28, and 4.06 by measured and calculated, respectively. Further, the magnetic properties of pure Fe_3O_4 NPs and sample 1-5 are investigated with an alternating gradient magnetometer at room temperature (Figure S2b). The magnetic saturation value was 54.89 emu g^{-1} for pure Fe_3O_4 NPs, and the magnetic saturation values of sample 1-5 are 5.39, 14.73, 26.40, 33.80 and 38.11 emu g^{-1} , respectively. The magnetic saturation value of a serial of Fe_3O_4 @GNS decreased gradually with the mass ratio of Fe_3O_4 to GO. Compared to that of as-prepared pure Fe_3O_4 NPs, the composites exhibit lower saturation magnetizations due to the presence of GNS. It was attributed to the addition of antiferromagnetic material (GNS) in Fe_3O_4 @GNS (Figure S2a). In order to confirm the crystal structures and phase components of the samples, XRD measurements were carried out, as shown in Figure 2. The characteristic diffraction peaks

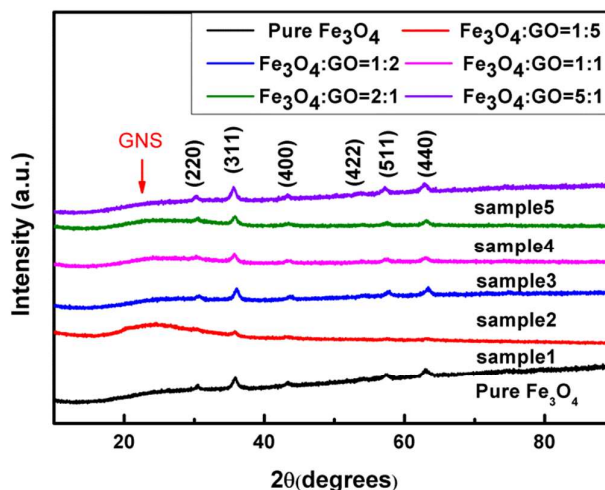


Figure 2 XRD patterns of pure Fe_3O_4 NPs and sample 1-5.

located at 30.1°, 35.5°, 43.1°, 53.4°, 56.9°, and 62.5° were indexed to (220), (311), (400), (422), (511), and (440) crystal planes of Fe_3O_4 . The structure of Fe_3O_4 corresponds to the cubic inverse spinel structure of magnetite (JCPDS card no. 19-0629). Comparing with pure Fe_3O_4 NPs, the crystalline structure of Fe_3O_4 in Fe_3O_4 @GNS does not change obviously after wrapped and thermally reduced. In addition, broad diffraction peak at 22.1° indexed to (002) plane of graphene can be clearly observed from sample 1-5. The above results indicate GNS warping layers have commendable protection effect for the thermal stability of Fe_3O_4 .

The morphologies of pure GNS and Fe_3O_4 @GNS with different Fe_3O_4 /GO ratios were shown in Figure 3 and Figure

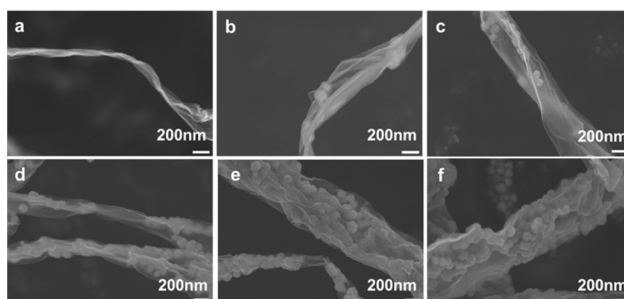


Figure 3 High magnification SEM images of (a) pure GNS, (b-f) sample 1-5.

S3, respectively. It can be seen that different amounts of Fe_3O_4 NPs intercalate into the galleries between GNS interlayers, and their morphologies and sizes of the Fe_3O_4 NPs do not significant change compared to that of pure Fe_3O_4 NPs. The loading amount of Fe_3O_4 NPs in GNS increased with the increase of Fe_3O_4 /GO ratios (Figure 2b-2f, Figure S3a-S3e). It is worth noting that the diameters of the Fe_3O_4 @GNS with different Fe_3O_4 /GO ratios gradually widens from sample 1 to sample 5 and the diameters range from 400 to 800 nm. Meanwhile, the lengths are not significant change from sample 1 to sample 4 but the length of sample 5 significantly became shorter. Sample 1-4 have the lengths ranging from 20 to 50 μm while the length of sample 5 is about 10 μm . For comparison,

the pure GNS was prepared by rolling up GO sheets following the previously reported processing (Figure 3a, S3a).³² It is worth noting that most GNS have the diameter about 100 nm and the lengths are similar to that of sample 1-4. In order to further investigation of morphologies and microstructures of the Fe_3O_4 @GNS with different Fe_3O_4 /GO ratios, TEM measurements were carried out shown in Figure 4. GNS do not

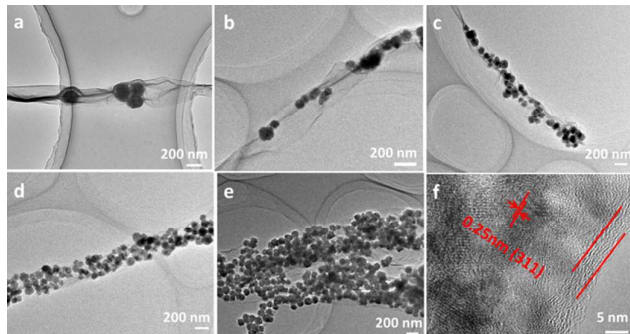


Figure 4 TEM images of (a-e) sample 1-5, (f) HR-TEM of sample 5.

entirely load with Fe_3O_4 NPs when the ratio of Fe_3O_4 to GO lower than 2 (Figure 4a-4c). Conversely, excessive amounts of Fe_3O_4 NPs were wrapped by GNS when Fe_3O_4 : GO=5:1 (sample 5) lead to the internal Fe_3O_4 NPs aggregate and cannot direct contact with graphene layers. The optimum structure was obtained when Fe_3O_4 : GO=2:1 (sample 4). Fe_3O_4 NPs were uniformly wrapped by GNS and directionally arranged like multi-particle-chain, which conform to “chain of spheres” model.^{37,38} This optimum structure realizes that Fe_3O_4 NPs were completely encapsulated and directly wrapped by GNS. And the conductivity of composites could be fundamental improved, more importantly, which insures the maximum loading amount of Fe_3O_4 NPs which been wrapped by GNS. For further investigation, it can be found that the single Fe_3O_4 nanoparticle is wrapped by graphene with thin layers (Figure 4f). The lattice spacing is about 0.25 nm, which is in good agreement with the (311) inter-planar distance of Fe_3O_4 , and the thickness of the graphene wrinkle or GNS wall is about 5~10 nm. Such a wrapped-linked morphology of GNS- Fe_3O_4 composites can reduce the particle-to-particle interface resistance by building continuous conductive paths and accommodating the volume change of the Fe_3O_4 NPs in LIBs cycle process.

The electrochemical performances of the as-prepared sample1-5 were evaluated by charge/discharge cycling in the voltage range of 0.01-3.0 V (vs Li/Li^+) at a current density of 100 mA g^{-1} (Figure. 5a). For comparison purposes, pure Fe_3O_4

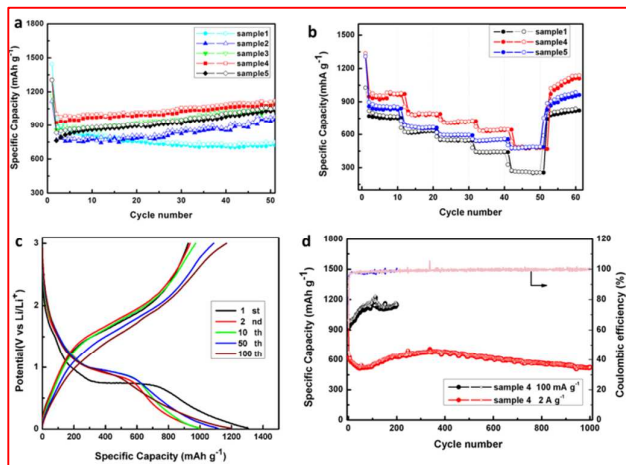
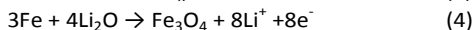
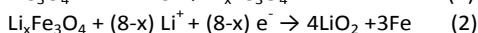


Figure 5 (a) Cycle performances of sample 1-5 at 100 mA g^{-1} , (b) Rate capabilities of these samples 1, 3 and 5 at $0.1\text{--}5 \text{ A g}^{-1}$, (c) The charging–discharging curves of sample 4 at 100 mA g^{-1} , (d) Cycle performances of sample 4 at 100 mA g^{-1} and 2 A g^{-1} .

NPs and GNS were also evaluated at the same test conditions (Figure S4). As the results shown, a serial of Fe_3O_4 @GNS electrodes present a much better cycling stability than that of the pure Fe_3O_4 NPs electrode, as well as a remarkably higher reversible capacity compared to pure GNS electrode. The initial discharge and charge capacities of the sample 1-5 are 1444 and $911.9 \text{ mA h g}^{-1}$, 1118 and $768.9 \text{ mA h g}^{-1}$, 1165.1 and 858 mA h g^{-1} , 1305.9 and $925.1 \text{ mA h g}^{-1}$, 1305 and $762.3 \text{ mA h g}^{-1}$, respectively, and the corresponding Coulombic efficiencies are 63%, 68%, 73%, 70% and 58%. The capacities of the sample 2-5 exhibit a gradual increase after second cycles. This phenomenon has been widely referred in both Fe-based transition metal oxides and other transition metal oxides, such as MnO , CoO and SnO_2 .³⁹⁻⁴¹ The most common explanation is that the trend of increasing reversible capacity may be attributed to the gradual improvement of lithium ion accessibility and the formation of a polymeric gellike film (PGF) which is caused by the decomposition of electrolyte during conversion process. Sample 1-5 display discharge capacities of 739.1 , 974.8 , 1080.9 , 1113.5 and $1049.5 \text{ mA h g}^{-1}$ after 50 cycles, respectively. In contrast, pure Fe_3O_4 and GNS only display discharge capacities of 176.1 and $499.5 \text{ mA h g}^{-1}$ after 50 cycles. The above results show that the LIBs performances of pure Fe_3O_4 and GNS are largely lower than that of Fe_3O_4 @GNS samples. For pure Fe_3O_4 electrode, the capacity fades rapidly after 50 cycles due to structure deterioration during the continuous volume expansion /contraction. The introduction of GNS into the composite improved the electrochemical performance of Fe_3O_4 . Sample 4 (Fe_3O_4 : GO=2:1) demonstrates the optimal cycling performance, which 85% capacity remained after 50 cycles. To further demonstrate the superior cycling stability of the sample 4 electrode, the cells were characterized by the galvanostatic discharge/charge cycling at different rates (figure 5d). It is worth noting that about 90% of the capacity is maintained after 200 cycles at a current density of 100 mA g^{-1} . Remarkably, at a current density of 2 A g^{-1} , the discharge capacity value of sample 4 decreased from $616.4 \text{ mA h g}^{-1}$ at the 6th cycle to $520.1 \text{ mA h g}^{-1}$ at the 48th cycle, but then increased to 692 mA h g^{-1} after the 340th cycle.

Even after 1000 cycles, sample 4 still maintained a specific capacity of 524 mAh g⁻¹. The initial decrease in the discharge capacity was related to that the completed transformation into a stable amorphous-like structure needed more cycling number during high rate cycling. In the following cycles the capacity was slowly increased caused by the completed transformation of the crystalline structure to a stable amorphous-like structure, thus enhancing the lithium insertion kinetics.⁴² The Columbic efficiency of sample 4 reached approximately 99% after the third cycle and was maintained at this value in the subsequent cycles at different current density. Figure 5c and Figure S5 show the galvanostatic charge/discharge curves of sample 1-5 and pure GNS and Fe₃O₄ over a potential range of 0.01-3 V at 100 mA g⁻¹. The discharge curves of pure Fe₃O₄ and sample 1-5 present a voltage plateau at ~0.7 V, which closely follows earlier reports on Fe₃O₄ anode materials.^{9,12,24} As described in eq 1,⁴³ with the formation of a solid electrolyte interphase (SEI) film. Meanwhile, the specific capacity of sample 2-5 increase gradually after 2 cycles, the reasons for this phenomenon we have explained in front of this section.



The CV for the first three successive cycles about pure Fe₃O₄, GNS and three typical as-prepared Fe₃O₄@GNS (less loads-sample 1, optimum structure-sample 4 and excess loads-sample 5) in the voltage range of 0.01 to 3.0 V at the scan rate of 0.1 mV s⁻¹ are displayed in figure 6. In the first cathodic scan

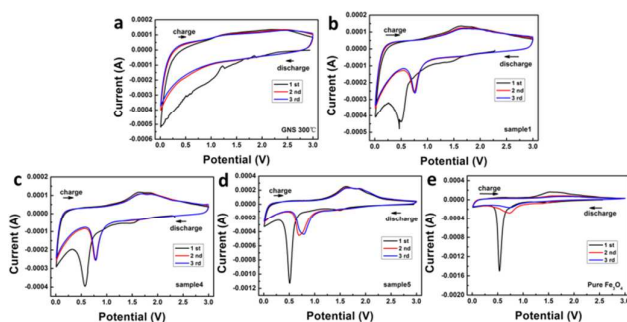


Figure 6 (a) Cyclic voltammetry profiles of pure GNS, (b) sample 1, (c) sample 4, (d) sample 5, and (e) pure Fe₃O₄ electrodes at 0.1 mV s⁻¹ scan rate.

stage, a strong reduction peak near 0.52V is obviously observed for both pure Fe₃O₄ NPs and three typical as-prepared Fe₃O₄@GNS, which corresponds to the reduction of Fe²⁺ and Fe³⁺ to Fe⁰ (eq 2),⁴³ as well as the formation of Fe clusters embedded in the Li₂O matrix together with decomposition of the organic electrolyte to form a SEI layer. In the first anodic sweep, the wide peak at about 1.77 V for pure Fe₃O₄, 1.86 V for sample1, 1.90 V for sample 4 and 1.91 V for sample 5 was ascribed to the oxidation of Fe⁰ to Fe²⁺ and Fe³⁺ (eq 4).⁴³ The slight peak shift from pure Fe₃O₄ to sample 1, 4 and 5 may be ascribed to the more oxidation of Fe⁰ to Fe³⁺, due to less aggregation, and more stable structure after GNS wrapping. The cathodic peak shifts to about 0.75 V in subsequent cycles consistently with other Fe₃O₄, or Fe₃O₄/C materials,⁴⁴ which may be attributed to structural modification

due to lithium insertion and extraction after the first cycle. Meanwhile, for the pure GNS and three typical as-prepared Fe₃O₄@GNS electrodes, the reduction peaks at 0.1V reflect lithium ion intercalation in GNS (eq 3).⁴³ More importantly, after the first cycle, compare to pure Fe₃O₄, the subsequent CV curves of three typical as-prepared Fe₃O₄@GNS anodes overlap very well, indicating the good cycling stability of the electrode.

Figure 5b shows the rate performance of three typical as-prepared Fe₃O₄@GNS samples (sample 1, 4 and 5). As the current density changed from 100 to 5000 mA g⁻¹, the specific capacities of 976.6, 791, 727.5, 648 and 480 mAh g⁻¹ were correspondingly obtained for sample 4 (optimum structure). When the current density is restored to the initial 100 mA g⁻¹, the specific capacity then increases back to 1138 mAh g⁻¹, indicating the outstanding rate capability of sample 4. And the reversible capacity is higher than the initial 10 cycles at the same current density, this result correspond to the previous reports. By contrast, the sample 1 and sample 5 electrodes exhibit low discharge capacities. Specially, the capacities of sample 1 sharply declined at high current density 5 A g⁻¹ which indicates less loading amounts of Fe₃O₄ NPs against the rate performances of LIBs. We also compare our results with other reported of the carbon-wrapped Fe₃O₄ nanoparticle, which are summarized in Table S1. It can be seen that the Fe₃O₄@GNS electrode is of excellent high-rate cycling performance.

The EIS of the electrodes for three typical as-prepared Fe₃O₄@GNS samples (sample 1, 4 and 5) and pure Fe₃O₄ were investigated (Figure. 7). As shown in Figure. 7, we clearly observed that the diameter of semicircle of sample 1, 4, 5 electrodes were much smaller than that of pure Fe₃O₄ electrode, which suggested that Fe₃O₄@GNS electrodes possess lower charge transfer resistances. These results confirmed that GNS wrapping layers could lead to high conductivity and enhanced electron transport. This greatly improved the activation and kinetics of conversion reaction upon lithium insertion/extraction.

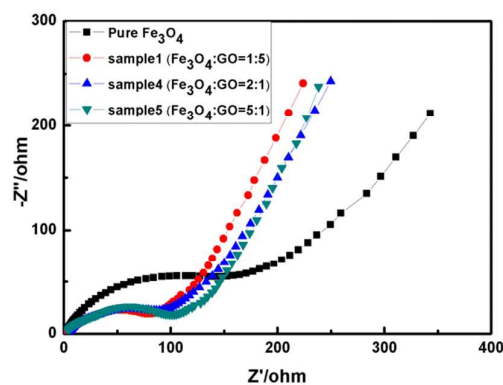


Figure 7 Electrochemical impedance spectra of the electrodes for sample 1, 4, 5 and pure Fe₃O₄.

Conclusions

In summary, a series of Fe₃O₄@GNS composites with different Fe₃O₄/GO ratios were prepared by cold quenching of the mixed suspensions of Fe₃O₄ NPs and GO in liquid nitrogen followed by thermal reduction. In all as-prepared composites, Fe₃O₄ NPs were tightly wrapped into the interlayer galleries of GNSs, resulting in the formation of 3D fibrous networks. More remarkably, in the sample of Fe₃O₄@GNS (Fe₃O₄: GO=2:1), Fe₃O₄ NPs wrapped by a GNS were directionally arranged like multi-particle-chain. Such novel structure is able to provide ideal anode characteristic for Li storage. Consequently, it exhibited outstanding cycling stability as well as excellent rate capability. These results make such Fe₃O₄@GNS as a promising anode candidate for high-performance LIBs.

Acknowledgements

This work was supported by the Foundation of Key Cultivation Project of Lanzhou Institute of Chemical Physics of The Chinese Academy of Sciences and Research Program of China and Natural Science Foundation of China (No. 21303234).

Notes and references

a. Laboratory of Clean Energy Chemistry and Materials, Lanzhou Institute of Chemical Physics, Chinese Academy of Sciences, Lanzhou 730000, P. R. China..

b. State Key Laboratory for Oxo Synthesis and Selective Oxidation, Lanzhou Institute of Chemical Physics, Chinese Academy of Sciences, Lanzhou 730000, P. R. China.

*Corresponding author. Tel.: +86-931-4968339; fax: +86-931-4968339. E-mail address: xushan@licp.cas.cn

Electronic Supplementary Information (ESI) available: [details of any supplementary information available should be included here]. See DOI: 10.1039/x0xx00000x

- 1 A. S. Arico, P. Bruce, B. Scrosati, J. M. Tarascon and W. Van Schalkwijk, *Nat. Mater.*, 2005, 4, 366-377.
- 2 K. Amine, I. Belharouak, Z. H. Chen, T. Tran, H. Yumoto, N. Ota, S. T. Myung and Y. K. Sun, *Adv. Mater.*, 2010, 22, 3052-3057.
- 3 K. Kang, Y. S. Meng, J. Bréger, C. P. Grey and G. Ceder, *Science*, 2006, 311, 977.
- 4 J. B. Goodenough and Y. Kim, *Chem. Mater.*, 2010, 22, 587.
- 5 J. M. Tarascon and M. Armand, *Nature*, 2001, 414, 359-367.
- 6 Y. Q. Zhu, C. Li and C. b. Cao, *RSC Adv.*, 2013, 3, 11860-11868.
- 7 G. M. Zhou, D. W. Wang, L.C. Yin, N. Li, F. Li and H. M. Chen, *ACS Nano*, 2012, 6, 3214-3223.
- 8 H. Liu, G. X. Wang, J. Liu and S. Z. Qiao, *J. Mater. Chem.*, 2011, 21, 3046-3052.
- 9 B. J. Li, H. Q. Cao, J. Shao, M. Z. Qu and J. H. Warner, *J. Mater. Chem.* 2011, 21, 5069-5075.
- 10 X. J. Zhu, Y. W. Zhu, S. Murali, M. D. Stoller and R. S. Ruoff, *ACS Nano*, 2011, 5, 3333-3338.
- 11 M. V. Reddy, Ting Yu, C-H Sow, Z. X. Shen, C. T. Lim, G. V. Subba Rao and B. V. R. Chowdari, *Adv. Funct. Mater.*, 2007, 17, 2792-2799
- 12 P. L. Taberna, S. Mitra, P. Poizat, P. Simon and J. M. Tarascon, *Nat. Mater.*, 2006, 5, 567-573.
- 13 J. Zhang, Y. Yao, T. Huang and A. Yu, *Electrochim. Acta.*, 2012, 78, 502-507.
- 14 Q. Zhang, Z. Shi, Y. Deng, J. Zheng, G. Liu and G.H. Chen, *J. Power Sources*, 2012, 197, 305-309.
- 15 P. Poizat, S. Laruelle, S. Grugeon, L. Dupont and J. M. Tarascon, *Nature*, 2000, 407, 496-499.
- 16 R. Teki, M. K. Datta, R. Krishnan, T. C. Parker, T. M. Lu, P. N. Kumta and N. Koratkar, *small*, 2009, 5, 2236-2242
- 17 Z. Y. Cao and B. Q. Wei, *ACS Appl. Mater. Interfaces*, 2013, 5, 10246-10252.

- 18 L. W. Ji, O. Toprakci, M. Alcoutlabi, Y. F. Yao, Y. Li, S. Zhang, B. K. Guo, Z. Lin and X. W. Zhang, *ACS Appl. Mater. Interfaces*, 2012, 4, 2672-2679.
- 19 W. M. Zhang, X. L. Wu, J. S. Hu, Y. G. Guo and L. J. Wan, *Adv. Funct. Mater.*, 2008, 18, 3941-3946.
- 20 B. J. Li, H. Q. Cao, J. Shao and M. Z. Qu, *Chem. Commun.*, 2011, 47, 10374-10376.
- 21 E. Yoo, J. Kim, E. Hosono, H. Zhou, T. Kudo and I. Honma, *Nano Lett.*, 2008, 8, 2277-2282.
- 22 M. D. Stoller, S. Park, Y. Zhu, J. An and R. S. Ruoff, *Nano Lett.*, 2008, 8, 3498-3502.
- 23 J. Z. Wang, C. Zhong, D. Wexler, N. H. Idris, Z. X. Wang, L. Q. Chen and H. K. Liu, *Chem. Eur. J.*, 2011, 17, 661-667.
- 24 G. M. Zhou, D. W. Wang, F. Li, L. L. Zhang, N. Li, Z. S. Wu, L. Wen, G. Q. Lu and H. M. Cheng, *Chem. Mater.*, 2010, 22, 5306-5313.
- 25 L. H. Zhuo, Y. Q. Wu, L. Y. Wang, J. Ming, Y. C. Yu, X. B. Zhang and F. Y. Zhao, *J. Mater. Chem. A*, 2013, 1, 3954-3960.
- 26 M. Sathish, T. Tomai and I. Honma, *J. Power Sources*, 2012, 217, 85-91.
- 27 C. D. Wang, Q. M. Zhang, Q. H. Wu, T. W. Ng, T. L. Wong, J. G. Ren, Z. C. Shi, C.S. Lee, S. T. Lee and W. J. Zhang, *RSC Adv.*, 2012, 2, 10680-10688.
- 28 L. M. Viculis, J. J. Mack and R. B. Kaner, *Science*, 2003, 299, 1361.
- 29 X. Xie, L. Ju, X. F. Feng, Y. H. Sun, R. F. Zhou, K. Liu, S. S. Fan, Q. Q. Li and K. L. Jiang, *Nano Lett.*, 2009, 9, 2565-2570.
- 30 J. Zheng, H. T. Liu, B. Wu, Y. L. Guo, T. Wu, G. Yu, Y. Q. Liu and D. B. Zhu, *Adv. Mater.*, 2011, 23, 2460-2463.
- 31 M. Y. Yan, F. C. Wang, C. H. Han, X. Y. Ma, X. Xu, Q. Y. An, L. Xu, C. J. Niu, Y. L. Zhao and X. C. Tian, *J. Am. Chem. Soc.*, 2013, 135, 18176-18182.
- 32 J. P. Zhao, B. J. Yang, Z. Yang, P. Zhang, Z. M. Zheng, W. C. Ren and X. B. Yan, *Carbon*, 2014, 79, 470-477.
- 33 J. P. Zhao, B. J. Yang, Z. M. Zheng, J. Yang, Z. Yang, P. Zhang, W. C. Ren and X. B. Yan, *ACS Appl. Mater. Interfaces*, 2014, 6, 9890-9896.
- 34 J. P. Zhao, S. F. Pei, W. C. Ren, L. B. Gao and H. M. Cheng, *ACS Nano*, 2010, 4, 5245-5252.
- 35 H. Deng, X. L. Li, Q. Peng, X. Wang, J. P. Chen and Y. D. Li, *Angew. Chem. Int. Ed.*, 2005, 44, 2782-2785.
- 36 F. P. Dong, W. P. Guo, J. H. Bae, S. H. Kim and C. S. Ha, *Chem. Eur. J.*, 2011, 17, 128 02-12808.
- 37 I. S. Jacobs and C. P. Bean, *Phys. Rev.*, 1955, 100, 1060-1067.
- 38 J. L. Zhang, J. C. Fu, G. G. Tan, F. S. Li, C. Q. Luo, J. G. Zhao, E. Q. Xie, D. S. Xue, H. L. Zhang, N. J. Mellors and Y. Peng, *Nanoscale*, 2012, 4, 2754-2759.
- 39 X. J. Jiang, Y. Y. Wang, L.S. Yang, D. W. Li, H. Y. Xu and Y. Ding, *J. Power Sources*, 2015, 274, 862-868.
- 40 R. H. Wang, C. H. Xu, J. Sun, L. Gao and H. L. Yao, *ACS Appl. Mater. Interfaces*, 2014, 6, 3427-3436.
- 41 X. Zhu, X. Y. Song, X. L. Ma and G. Q. Ning, *ACS Appl. Mater. Interfaces*, 2014, 6, 7189-7197.
- 42 J. Lin, A. O. Raji, K. W. Nan, Z. W. Peng, Z. Yan, E. G. Samuel, D. Natelson and J. M. Tour, *Adv. Funct. Mater.*, 2014, 24, 2044-2048.
- 43 S. Saadat, J. Zhu, D. H. Sim, H. H. Hng, R. Yazami and Q. Y. Yan, *J. Mater. Chem. A*, 2013, 1, 8672-8678.
- 44 D. Li, X. W. Li, S. Y. Wang, Y. X. Zheng, L. Qiao and D. Y. He, *ACS Appl. Mater. Interfaces*, 2014, 6, 648-654.23.